UNIVERSITY OF LEEDS

This is a repository copy of *Release of tephra-hosted iron during early diagenesis fingerprinted by iron isotopes*.

Version: Accepted Version

White Rose
university consortium
Universities of Leeds, Sheffield & York

eprints@whiterose.ac.uk
https://eprints.whiterose.ac.uk/

Release of tephra-hosted iron during early diagenesis fingerprinted by iron isotopes

Jack Longman[1*†], Ann G. Dunlea[2], Philipp Böning[1], Martin R. Palmer[3], Thomas M. Gernon[3], James McManus[4], Hayley R. Manners[5], William B. Homoky[6], Katharina Pahnke[1]

[1]Marine Isotope Geochemistry, Institute for Chemistry and Biology of the Marine Environment (ICBM), University of Oldenburg, Oldenburg, Germany

[2]Woods Hole Oceanographic Institution, Woods Hole, MA, USA.

[3]School of Ocean and Earth Sciences, University of Southampton, Southampton, UK

[4]Bigelow Laboratory for Ocean Sciences, East Boothbay, ME, USA.

[5]School of Geography, Earth and Environmental Sciences, University of Plymouth, Plymouth, UK.

[6]School of Earth and Environment, University of Leeds, Leeds, UK

[*]Corresponding author: jack2.longman@northumbria.ac.uk

[†] Present address: Department of Geography and Environmental Sciences, Northumbria University, Newcastle-upon-Tyne, UK

Abstract

The micronutrient iron (Fe) plays a fundamental role controlling primary productivity in the upper ocean, with volcanic eruptions and deposition of airborne volcanic material (termed tephra) a potential source of Fe. Here, we investigate the geochemical and Fe isotopic (δ^{56}Fe) composition of tephra layers, sediments, and mixed tephra-sediment samples from the Integrated Ocean Drilling Program (IODP) Hole 1396C, located offshore the volcanically active island of Montserrat in the Lesser Antilles, Caribbean Sea. We find that buried tephras, which have experienced diagenesis, exhibit lighter δ^{56}Fe (relative to standard IRMM-524a) compositions (down to -0.26 ± 0.04‰, 2SD) than fresh tephra deposited in Montserrat (δ^{56}Fe = 0.02 ± 0.02‰, 2SD). Such negative values suggest that isotopically heavier Fe has been lost from the originally deposited material. Using multivariate statistical modelling and mass balance constraints, we identify the outward Fe flux (with calculated δ^{56}Fe of 0.21 ± 0.31‰, 2SD, n=12) during non-reductive dissolution of tephra as the likely cause of the retention of these light δ^{56}Fe compositions. Due to the widespread nature of tephra deposition, tephra diagenesis may provide an important source of isotopically heavy dissolved Fe (dFe) to the oceans. This process contrasts with more commonly considered reductive dissolution processes, which provide a source of dFe enriched in light isotopes to the oceans.

1. Introduction

As an essential micronutrient for phytoplankton photosynthesis, dissolved iron (dFe) Fe)availability is directly linked to primary productivity and plankton community structure in modern high-latitude oceans (Falkowski et al., 1998; Kolber et al., 1994; Martin and Fitzwater, 1988; Tagliabue et al., 2017). Because primary productivity is one of the most important mechanisms determining air-sea CO_2 exchange, understanding Fe biogeochemistry is key to understanding marine carbon cycling (Tagliabue et al., 2017).

Dissolved (<0.2 µm) and particulate (>0.2µm) Fe is supplied to the ocean via rivers, aeolian deposition, hydrothermal vents and remobilization of sediment-hosted Fe (Homoky et al., 2013; Johnson et al., 2020; König et al., 2021). In addition, volcanism, and especially the eruptive dispersal of tephra, may provide an important episodic input of particulate Fe (pFe) to the Earth's surface environment (Longman et al., 2022; Olgun et al., 2011). Explosive volcanism results in the total eruption of ~1 km^3 of tephra (or unconsolidated pyroclastic material including pore space) every year (Pyle, 1995), and because most volcanoes are located on islands or near continental margins, as much as 45% of this tephra enters the ocean (Longman et al., 2022). Upon entering the ocean, tephra reacts rapidly with seawater, releasing of macro- and micro-nutrients such as dFe (Frogner et al., 2001; Jones and Gislason, 2008). A first estimate of the scale of this nutrient supply indicates tephra may deliver between 50 – 500 Gmol yr^{-1} of dFe to the oceans, with a median value of 180 Gmol yr^{-1} (Longman et al., 2022). The dFe delivery associated with tephra could therefore alleviate nutrient deficiencies for phytoplankton in Fe-limited regions of the ocean (Achterberg et al., 2013; Duggen et al., 2010; Moore et al., 2013; Olgun et al., 2013). Further, the release of other micronutrients such as dissolved Mn during this process mean tephra may also supply other co-limiting nutrients (Browning et al., 2021, 2014; Longman et al., 2020). The magnitude of this dFe source is also highlighted by the observation that roughly 30% of Pacific sediment located close to (i.e., within 1000km) of active arcs is comprised of tephra (Scudder et al., 2014, 2009). While the potential importance of tephra for oceanic Fe budgets is clear, the release of dFe during the diagenetic alteration of this volcanic material is poorly constrained and not yet represented

57 in the Fe-cycle parameterisation of any global ocean biogeochemical models (König et al., 2021;

58 Tagliabue et al., 2016).

59 One method for investigating the cycling of Fe in the ocean uses its isotopic composition, typically

60 presented as $\delta^{56}Fe$ relative to a measured standard. This composition can help trace the sources, sinks

61 and cycling of Fe between the oceans and sediments (Conway and John, 2014; Homoky et al., 2013;

62 Radic et al., 2011), provided the external sources of dFe and pFe to the oceans and the processes that

63 fractionate Fe isotopes within and between them are understood (Johnson et al., 2020).

64 Typically, sources of dFe to the ocean such as dust and dFe released from oxic sediment, have isotopic

65 signatures close to crustal values (0.09 ± 0.07‰; Beard et al., 2003). However, these compositions may

66 be modified in parts of the ocean influenced by variable redox conditions (Johnson et al., 2020). For

67 example, in low-oxygen sedimentary environments, reductive dissolution of Fe (a product of

68 dissimilatory microbial reactions) leads to the release of dFe to porewaters with negative $\delta^{56}Fe$

69 compositions, with values reaching as low as -3.3‰ (Homoky et al., 2009). Hydrothermal vent fluids

70 typically have $\delta^{56}Fe$ between -0.1 to -0.5‰ (Bennett et al., 2009; Johnson et al., 2020), but can be

71 modified by the precipitation of sulfides or oxides. These precipitation reactions occur when either of

72 the species are saturated in the fluids, and authigenic precipitates preferentially incorporate lighter

73 isotopes when sulfides form and heavier isotopes when oxides form, thereby fractionating the remnant

74 dFe in the fluid (Lough et al., 2017).

75 In addition to these reductive dissolution pathways, heavy ($\delta^{56}Fe > 0‰$) lithogenic Fe signatures have

76 been observed in porewaters (Homoky et al., 2021, 2013, 2009) and seawater (Conway and John, 2014;

77 Radic et al., 2011) in some deep water locations. These heavy dFe values have been attributed to non-

78 reductive dissolution (NRD) of lithogenic material in oxidising sediments, and indicates these oxic

79 sediments may be an additional source of dFe to the oceans (Abadie et al., 2017; Homoky et al., 2013;

80 König et al., 2021). This process, via the production of organo-mineral Fe colloids <0.2 μm in size,

81 may provide a mechanism by which lithogenic $\delta^{56}Fe$ compositions are added to the ocean interior from

82 oxidising margins (Homoky et al., 2021). Notably, the oxidative weathering of volcanoclastic marine

83 sediments containing organic carbon between 0.3 – 0.6 % has produced the highest porewater

84 concentrations of dFe with crustal isotope compositions observed so far (Homoky et al., 2021),

85 indicating these volcanogenic sediments could provide a uniquely important source of dFe for the

86 ocean.

87 Here, we present Fe isotopic compositions from sediments, tephras and mixed sediment-tephra layers

88 from offshore Montserrat in the Caribbean Sea to estimate the Fe isotopic composition of Fe lost during

89 tephra transport and diagenesis. We combine these data with multivariate partitioning methods and

90 calculations of the depletion factors and mass balance calculations to estimate the isotopic composition

91 of Fe supplied to the ocean via dissolution of tephra during water column transport and early diagenesis.

2. Material and Methods

2.1. Study Site, Sampling and Age Model

94 Integrated Ocean Drilling Program (IODP) Hole 1396C was drilled as part of Expedition 340 in August-

95 September 2012 (Le Friant et al., 2013). It is located ~30 km west of Montserrat at 16°30.5′N,

96 62°27.1′W (Fig. 1), and was drilled to a depth of 139.4 m below seafloor (mbsf). The core is carbonate-

97 dominated, with abundant tephra layers and a minor contribution from terrigenous sediments. Bulk

98 marine sediment and visually distinct discrete tephra layers were both sampled. For the samples from

99 the tephra layers, efforts were made to sample from the centre of the layer to attain a purely volcanic

100 signal. In addition to the IODP samples, we also studied fresh tephra from the 8th January 2010 eruption

101 of the Soufrière Hills volcano, Montserrat.

2.2. Elemental analysis

103 Freeze-dried and homogenized tephra (n = 18) and sediment (n = 44) samples were dissolved using a

104 mixed acid (HCl-HF-HNO$_3$) benchtop method. Solutions were diluted 1:5000 and analysed using a

105 Thermo X-Series at the University of Southampton following the protocol of Longman et al. (2022).

106 The certified reference material HISS-1 (sandy marine sediment), and procedural blanks were prepared

107 and analysed in the same manner. For this work, a full suite of major and trace elements was analysed.

108 Blank content was shown to be negligible for all elements, and recoveries for HISS-1 were within 10%

109   of expected values for most elements (see Supplementary Table 1). For Fe, two measurements of HISS-

110   1 marine sediment standard averaged 2950 ppm, with an expected value of 2460 (recovery 97%). Blanks

111   for Fe were on average 0.66 ppm, or 0.02% of the standard material. Porewater analysis of Fe was

112   completed using the method of Murray et al. (2016). Briefly, pore waters were diluted to a 1:20 ratio

113   using 1% distilled nitric acid before analysis on a Leeman Labs Prodigy ICP-OES at Oregon State

114   University. The fresh tephra was analysed via X-Ray Fluorescence (Panalytical Axios Max) analysis at

115   the University of Oldenburg. 700mg of sample was mixed with 4200 mg of Li-tetraborate, pre-oxidised

116   at 500 °C with NH_4NO_3 and fused to form a glass bead. The in-house standard PS-S was prepared an

117   analysed in the same manner. Fe_2O_3 content in the measured standard was 4.72%, compared to a long-

118   term average of 4.76%, with repeat measurements within 0.1% of each other (n=3). In addition to the

119   in-house standard, three certified reference materials (BE-N, JB-2 and SDO1) were prepared and

120   analysed, with measured values of Fe_2O_3 close to certified values (see Supplementary Table 2).

121   ## 2.3.   Carbon analyses

122   Total organic carbon (TOC) measurements were made at Oregon State University following the method

123   of Goñi et al. (2003), as reported in Murray et al. (2016). Further details on methods, blanks and

124   reproducibility can be found in Murray et al. (2016).

125   ## 2.4.   Fe isotope analysis

126   A portion of the samples analysed for major and trace elements, and the fresh tephra samples, were

127   analysed for their Fe isotope composition (n = 20). Samples were homogenized using an agate pestle

128   and mortar prior to digestion of around 25 mg of sample via a mixed acid (HNO_3-$HClO_4$-HF) closed-

129   vessel approach (Böning et al., 2004). Blanks and certified reference materials were dissolved in the

130   same manner as samples. Aliquots of the digested samples were then purified via column chemistry

131   (Böning et al., 2020; Dauphas et al., 2009). Samples were taken up in 6M HCl and Fe separation was

132   performed using 1.8 mL AG1X8 anion resin (100–200 mesh, Bio-Rad) loaded onto PP columns (Bio-

133   Rad). After separation, samples were treated with H_2O_2 to remove any organic compounds leached from

134   the columns, before drying. All purification was completed using ultra-clean acids in the clean

135   laboratory facilities of the ICBM, University of Oldenburg.

136   Purified samples were diluted (to 3% HNO_3 and 3.3 ppm Fe) and analysed using a Thermo-Scientific

137   Neptune *Plus* multi-collector inductively coupled plasma mass spectrometer (MC-ICP-MS) at the

138   ICBM, Oldenburg. NIST 986 (National Institute of Standards and Technology, USA), a certified Ni

139   isotope standard, was quantitatively added to each sample and standard for mass bias correction of up

140   to 0.1 ‰ (Oeser et al., 2014). Signal intensity was ~15V for Fe and ~3V for Ni. Interference of ^{54}Cr on

141   ^{54}Fe was monitored and corrected using ^{52}Cr (Weyer and Schwieters, 2003). Analysis of each sample

142   was bracketed by a repeat standard (IRMM-524a), which is indistinguishable (within experimental

143   uncertainty) from the more widely used isotope standard IRMM-14 (González De Vega et al., 2020).

144   All results and comparisons to the literature are reported in delta notation relative to the mean of repeat

145   IRMM-524 values (n = 112):

146      $\delta^{56}Fe$ (‰) = [($^{56}Fe/^{54}Fe_{sample}$)/($^{56}Fe/^{54}Fe_{IRMM-524}$)] * 10^3

147   The reference materials SDO-1 (Devonian shale, US Geological Survey), BHVO-2 (Hawaiian basalt,

148   US Geological Survey) and HISS-1 (marine sandy sediment, National Research Council of Canada)

149   were used to assess the accuracy of Fe separations and measurements. Measurements of SDO-1 ($\delta^{56}Fe$

150   = 0.027 ± 0.017‰, n = 10, two digests, 2SD) were in good agreement with published values of 0.023 ±

151   0.028‰ (Schoenberg and Von Blanckenburg, 2005), and 0.026 ± 0.045‰ (Böning et al., 2020).

152   Measurements of BHVO-2 ($\delta^{56}Fe$ = 0.078 ± 0.041‰, n = 3, 2SD) were within error of previously

153   published values of 0.121 ± 0.049‰ (Liu et al., 2014), and 0.100 ± 0.060‰ (Foden et al., 2018).

154   Procedural blanks were negligible (<0.1% of total Fe in the lowest concentration sample).

2.5. Numerical analysis

2.5.1. Multivariate Partitioning

157 We used a series of multivariate techniques to determine the sediment provenance and the relative

158 contribution of each source to the sediment mixture deposited at Hole U1396C. First, we assessed the

159 relationships between element concentrations with r^2 matrices, x versus y element plots, and ternary

160 plots to identify trends, outliers, and simple covariation patterns. Second, we selected elements in the

161 dataset that were predominantly affiliated with the aluminosilicate fraction of the sediment and applied

162 Q-mode Factor Analysis (QFA; Pisias et al., 2013). To ensure the robustness of the QFA results, we

163 tested many combinations of elements, ran iterations with sample outliers removed, and assessed the

164 sensitivity of the results when an additional factor was added or subtracted. Furthermore, we selected

165 elements that were unique from those used in our tephra depletion model (Zr, Ti; see below) to

166 determine if an independent technique produced similar results. Guided by the x versus y plots, ternary

167 diagrams, and QFA results, elements and end-members were selected on the basis that they could be

168 statistically differentiated in the dataset. The element concentration data were then modelled using

169 constrained-least squares multiple linear regression (CLS; Pisias et al., 2013; Dunlea et al., 2015;

170 Dunlea and Murray, 2015).

171 In the CLS mixing models, thousands of combinations of possible end-members from published studies

172 or discrete layers measured in this study were tested to best fit the geochemical dataset in this study.

173 The CLS model aims to minimize the difference between the model and measured data. Our preferred

174 model was selected based on the strength of correlation coefficients of the CLS model and our

175 geological knowledge of which sediment sources would feasibly be found at Hole U1396C (see

176 Supplementary Tables 6-10; Supplementary Text).

2.5.2. Tephra Fe depletion calculations

178 We used two approaches to calculate early diagenetic Fe depletion factors for samples that were tephra-

179 rich (>75% tephra contribution as estimated from the CLS model): Zr-normalization after Lee et al.

180 (2018), and a multivariate CLS model. Zr-normalization compares the Fe/Zr and Ti/Zr ratios of the

181 analysed ashes to a reference dataset of Caribbean volcanic rocks, derived from the GeoROC database

182 (c.f. Longman et al., 2021; Longman et al., 2022). Data were downloaded from https://georoc.eu/, with

183 all original publications and the specific search terms listed in the Supplementary Text. Here, Zr and

184 Zr/Ti are assumed to be immobile whereas Fe may be mobilised during early diagenesis (Lee et al.,

185 2018). The linear regression between the Fe/Zr and Ti/Zr of the igneous rock dataset is interpreted to

186 represent the unaltered protolith of the tephra analysed here (Supplementary Figure 1). Using this

187 relationship and the measured Ti/Zr of the tephra layers, an original Fe/Zr composition can be back

188 calculated, and depletion factors (DF) estimated, using the following equation:

189
$$DF_{Fe} = \frac{M_{Fe}^L}{M_{Fe}^O} = 1 - \frac{\left(\frac{C_{Fe}^{re}}{C_{Zr}^{re}}\right)}{\left(\frac{C_{Fe}^O}{C_{Zr}^O}\right)} \quad (Eq.\,1)$$

190 Where the left side of the equation is the Fe depletion factor, DF_{Fe} (in %), with M_{Fe}^O the original Fe

191 mass in the protolith and with M_{Fe}^L the mass of Fe lost from the protolith C_{Fe}^{re} and C_{Zr}^{re} are the mass

192 concentrations of Fe and Zr in analysed tephra, and C_{Fe}^O / C_{Zr}^O represents the Fe/Zr ratio of the protolith.

193 All masses are in wt%, with oxide content corrected where necessary.

194 A second approach, based on the end-member compositions and mass fractions from the CLS model

195 was also applied to the discrete tephra layer and bulk sediment samples. The mass fraction of each end-

196 member within each sample was multiplied by the concentration of Fe in that end-member. Summing

197 the contributions of Fe from each end-member provides an estimate of how much Fe is expected in each

198 sample if no Fe had been lost from the original tephra composition. As such, the total measured Fe in

199 the sample can be subtracted from the predicted Fe content to obtain a depleted fraction:

200
$$f_{EM1}*[Fe]_{EM1} + f_{EM2}*[Fe]_{EM2} + f_{EM3}*[Fe]_{EM3} = Total\ [Fe]_{tephra} \quad (Eq.\ 2)$$

201 where f_{EM} = the fraction (0-1) of an end-member present in tephra. The difference between the predicted

202 total Fe concentration in tephra (Total [Fe]$_{tephra}$) and the independently measured Fe content in tephra

203 and sediment samples provides an estimate of the total Fe (wt. %) lost or gained during early diagenesis.

3. Results and Discussion

3.1. Sources of sediment in Hole U1396C

206 The multivariate statistical analyses identified three end-members defined from the major and trace

207 metal dataset in the aluminosilicate fraction (i.e., non-carbonate component) of sediment at Hole

208 U1396C. Because the Al and Ti concentrations are much higher than the concentrations of the other

209 trace elements, they have more influence on the outcome of the model. For example, the magnitude of

210   a small variation in Al can still be much larger than a relatively significant variation in Nb. To avoid

211   this bias toward higher concentration elements, we did not use Al and Ti in the CLS model and instead

212   relied on elements in the ppm range. The factor analysis suggests that three aluminosilicate components

213   can be distinguished with or without Al and Ti included. In our preferred model, the QFA uses a

214   combination of trace and rare earth elements (Co, Nb, Y, La, Ce, Eu, Yb, and Th) to explain 97% of the

215   data variability with three factors (Fig. 2). The first aluminosilicate factor identified in the QFA

216   explained 45% of the variability in the dataset and indicated a strong covariance (i.e., high VARIMAX

217   factor scores) among Nb, La, Ce, and Th throughout the samples (Fig. 2). The second factor explained

218   36% of the variability of the dataset and indicated a strong covariance among Y, Ce, Eu, and Yb. The

219   third factor explained 16% of the dataset and showed a covariance between Co and Eu.

220   After testing thousands of different combinations of end-members in the CLS model to find the best fit

221   for these element concentrations (Dunlea and Murray, 2015), QFA Factors 1 – 3 were interpreted to

222   represent a continental dust source and two andesitic tephra end-members, respectively. In the CLS

223   model, a continental dust end-member was chosen to approximate the composition of upper continental

224   crust (Rudnick and Gao, 2013). This interpretation is in accord with previous studies that show Saharan

225   dust forms a minor component of marine sediments in this area (Reid et al., 1996). The first andesitic

226   tephra with a more felsic composition used in the model was a discrete tephra layer measured in this

227   study (134.63 mbsf at Site U1396), but was also represented well by a subaerial tephra from Montserrat

228   (Sample 11.1.4C from Coussens et al., 2017). The second andesitic tephra end-member with a more

229   mafic composition than the other andesitic tephra layers is represented best by a tephra composition

230   from the Las Sierra volcanoes in Nicaragua (Schindlbeck et al., 2018), but the composition is also

231   similar to a subaerial tephra from Monserrat (Sample 9.2.1E from Coussens et al., 2017). Based on its

232   proximity, subaerial tephra from Montserrat was selected as the more likely for Site U1396C (Fig. 3).

233   Previous work offshore Montserrat has indicated that sediments are a three-component mixture

234   (terrestrial, $CaCO_3$ and tephra) and that Cr depletion can be used as a proxy for tephra content (Peters

235   et al., 2000; Scudder et al., 2016). Our approach builds on this normative calculation, as it considers a

236   range of elements. Our findings support previous work that indicates much of the tephra in marine

237   sediments is not in discrete layers, but is in the 'dispersed' tephra component (Peters et al., 2000;

238   Scudder et al., 2009; 2014). That is, tephra that has undergone some form of mixing process (e.g.

239   bioturbation, transport in the water column) is not visible in sediment cores as discrete layers (Scudder

240   et al., 2009; 2016). As expected, with 'tephra layers' (identified as layers with $CaCO_3$ <10 wt.%), the

241   tephra component is typically >85 wt.% (89 ± 13 wt.%, 1SD, n = 18). However, in the bulk sediment

242   samples, the combined andesite tephra (i.e., the dispersed tephra component) contribution remains high

243   (29 ± 10 wt.%, 1 SD, n = 43), with a maximum of 55 wt.% (Fig. 3). An average of 29 wt.% is higher

244   than the previous upper estimate of dispersed tephra in this region's sediment (between 15 – 20 wt.%;

245   Peters et al., 2000), and confirms the importance of tephra deposition in Caribbean sediments.

246   3.2. Fe isotope systematics

247   The $\delta^{56}Fe$ values in tephra-rich samples from U1396C range from -0.26 to 0.01 ‰, with an average of

248   -0.12 ± 0.08 ‰ (1SD, n = 19). 18 of 19 samples fall outside of the range of crustal rocks (0.09 ± 0.07

249   ‰, as defined by Beard et al. 2003), and none have a $\delta^{56}Fe$ composition higher than these crustal rocks

250   (Fig. 4; Supplementary Table 3). Our measured Fe isotope value of terrestrial tephra on Montserrat

251   ($\delta^{56}Fe$ = -0.019 ± 0.02‰) is within the envelope of crustal rock compositions, and similar to previous

252   measurements of volcanics from the Lesser Antilles , which yielded a $\delta^{56}Fe$ value of 0.045 ± 0.039‰

253   (Foden et al., 2018). These measurements on the Lesser Antilles volcanics were completed on lava

254   samples from onshore outcrops, and so the comparability between the two values suggests little Fe

255   isotope fractionation occurs during the eruption of explosive volcanic products in the Lesser Antilles

256   arc. While airborne transport may alter Fe speciation (Maters et al., 2017) and total Fe content of the

257   tephra (Simonella et al., 2015), atmospheric processes do not significantly alter the Fe isotope

258   composition of the tephra.

259   Measurements of marine sediment and tephra samples from Hole U1396C, show considerable variation

260   from what may be considered a magmatic rock Fe isotope composition, with subaerial volcanic rock

261   isotope compositions typically between −0.054 and 0.1 ‰ (Foden et al., 2018; Johnson et al., 2020).

262   Thus, our data indicate that some process within the tephra-rich sediments leads to more negative $\delta^{56}Fe$

263   values in the tephras recovered from marine sediments than observed in subaerial volcanic rocks. This

264   process may involve a diagenetic reaction, admixture of other sedimentary sources with distinct Fe

265   isotopic compositions, and/or interaction with dFe from seawater.

266   To investigate the possibility that the total isotopic composition ($\delta^{56}Fe_{Total}$) reflects the mixture of tephra

267   with terrigenous and carbonate contributions, we assume the isotopic composition is governed by the

268   mass-balance of these sources ($\delta^{56}Fe_{ash}$, $\delta^{56}Fe_{terr}$ and $\delta^{56}Fe_{carb}$, respectively; Eq. 3):

269 $$\delta^{56}Fe_{Total} = (\delta^{56}Fe_{Tephra} \times f_{Tephra}) + (\delta^{56}Fe_{terr} \times f_{terr}) + (\delta^{56}Fe_{Carb} \times f_{carb}) \text{ (Eq. 3)}$$

270   Where f is the molar fraction of each component. However, there is no evidence for any Fe-rich

271   carbonates (such as siderite) in the Caribbean Sea, and only aragonite and Mg-rich carbonate have been

272   reported (Reid et al., 1996), hence this fraction is likely to contain low levels of Fe (Fe/Ca of below 30

273     $\mu mol\ mol^{-1}$; see Boyle, 1981). Any Fe associated with the biogenic carbonate will be present only in

274   the form of Fe-Mn diagenetic coatings (Boyle, 1981). Further, chemical extractions used to detect the

275   presence of Fe-carbonates in marine sediments adjacent to Montserrat also confirmed at most only trace

276   abundances (<0.02 dwt % of total sediment or <0.5 dwt% of total Fe; Homoky et al., 2011). As such,

277   we consider the carbonate contribution to the isotopic mixture to be negligible, and so simplify the

278   equation as follows (Eq. 4):

279 $$\delta^{56}Fe_{Total} = (\delta^{56}Fe_{Tephra} \times f_{Tephra}) + (\delta^{56}Fe_{terr} \times f_{terr}) \text{ (Eq. 4)}$$

280   We can use our measured estimate of $\delta^{56}Fe$ for terrestrial tephra (-0.019 ± 0.023 ‰; $\delta^{56}Fe_{Tephra}$),

281   published estimates of the $\delta^{56}Fe$ of terrigenous material (c. 0.01 ± 0.05 ‰; $\delta^{56}Fe_{Terr}$, Beard et al., 2003),

282   and the proportion estimates for tephra (combining the contribution of the two andesites) and

283   terrigenous material (f_{Ash}, f_{Terr}) from the CLS model to assess if a simple mixture may explain the

284   measured Fe composition in our samples. Using the values of $\delta^{56}Fe_{Tephra}$ and $\delta^{56}Fe_{Terr}$ and the error

285   defined above, the most negative $\delta^{56}Fe$ composition produced by these mixtures is -0.043‰

286   (significantly more positive than most of the samples measured from U1396C).

287   One of the key diagenetic processes that acts on tephra in marine sediment is dissolution and leaching

288   (Jones and Gislason, 2008; Longman et al., 2019). Here, we focus on those 12 samples containing >75

289   wt.% ash (the closest representatives of 'pure' tephra samples within our sample suite) to test whether

290   diagenesis favours the loss of heavy Fe isotopes and the retention of isotopically light (δ^{56}Fe lower than

291   -0.1‰) Fe in the sediment. In this mass balance calculation, we assume that the measured δ^{56}Fe

292   (δ^{56}Fe$_{Measured}$) is the result of the modification of the original tephra, with the dFe lost through early

293   diagenesis represented by the proportion f_{Lost}. In this scenario, the $\delta^{56}Fe_{Measured}$ comprises the following

294   mass balance (Eq. 5):

295 $$\delta^{56}Fe_{Measured}= (\delta^{56}Fe_{Tephra} \times f_{Tephra}) - (\delta^{56}Fe_{Lost} \times f_{Lost}) \text{ (Eq. 5)}$$

296   The calculated $\delta^{56}Fe_{Lost}$ values, are considered representative of the isotopic composition of the Fe lost

297   during early diagenesis, and f_{Lost} is the proportion of Fe that was lost from the protolith. f_{Lost} can be

298   estimated using depletion factor (DF$_{Fe}$) calculations (see Methods and Materials), which estimate how

299   much Fe has been lost. Firstly via a Zr depletion model as detailed in Lee et al. (2018), and secondly

300   via a CLS-based model, using outputs from the multivariate partitioning. Therefore, f_{Tephra} is calculated

301   by subtracting f_{Lost} from 1. By rearranging equation 5, and using these independent DF$_{Fe}$ estimates as

302   f_{Lost}, we can solve for δ^{56}Fe$_{Lost}$ as follows:

303 $$\delta^{56}Fe_{Lost}= (\delta^{56}Fe_{ash} \times f_{Tephra}) - (\delta^{56}Fe_{Measured})/f_{Lost} \text{ (Eq. 6)}$$

304   As we use two methods to estimate DF$_{Fe}$, we derive two estimates for δ^{56}Fe$_{Lost}$ (see Fig. 5), but they are

305   in good agreement (Supplementary Figure 2), with significant correlation between the two ($r^2 = 0.65$,

306   p-value 0.02, n = 12). Although the estimated ranges of f_{Lost} vary between our DF$_{Fe}$ methods (Zr

307   normalization model-12 to 80%, CLS Model -3 to 54%,), both approaches yield similar results and

308   suggest net positive values for δ^{56}Fe$_{Lost}$ relative to the original isotopic composition of the tephra. A

309   single sample appears to have gained Fe through diagenesis, potentially through reprecipitation of Fe-

310   bearing phases, reflected in the negative model result (Fig. 5). The results derived from Zr-normalization

311   show slightly higher mean values for δ^{56}Fe$_{Lost}$ (0.36 ± 0.28‰, 1SD, n = 12) within uncertainty of the

312   mean value derived from our CLS modelling approach (0.21 ± 0.15‰, 1SD, n=12). These positive

313   values for δ^{56}Fe are similar to measurements of dFe supplied to porewater and seawater via non-

314   reductive dissolution (NRD), as inferred in oxidizing pore water δ^{56}Fe from tephra-rich sediments near

315   the Crozet Islands (0.16 ± 0.05‰; Homoky et al., 2009), the Cape Margin (0.22‰; Homoky et al.,

316   2013), western South Atlantic (δ^{56}Fe = 0.07 ± 0.07‰; Homoky et al., 2021) and New Guinea Coastal

317   waters (0.37 ± 0.15‰; Radic et al., 2011).

318   It is assumed that NRD does not derive from a chemical reaction specifically for Fe — rather the release

319   of Fe following the physical and chemical weathering of primary host-silicate structures – a process

320   that by itself should not fractionate Fe isotopes. However, the chelation of ferric ions by organic ligands

321   is known to favour heavier Fe isotopes, with fractionation factors of between +0.2 to +0.5‰ observed

322   experimentally (Dideriksen et al., 2008; Morgan et al., 2010), and in the natural environment (Ilina et

323   al., 2013). Ligand-complexation is also used to explain dissolved δ^{56}Fe values in North Atlantic surface

324   waters that are +0.2 to +0.6‰ higher than the pFe source in Saharan dust (Conway and John, 2014).

325   The fractionation effect attributed to NRD of pFe elsewhere in the ocean interior is shown to be on

326   average +0.2‰ enriched in the dissolved pool (Radic et al.,2011; Labatut et al., 2014; Abadie et al.,

327   2017). Therefore, it is likely the isotopic fractionation of f_{Lost} observed in our analysis represents the

328   primary signature from NRD of tephra, and any physicochemical transformations to more stable

329   dissolved phases. These transformations may involve ferric ion chelation by organic ligands, and/or the

330   precipitation and stabilisation of colloidal Fe (oxyhydr)oxides with organic carbon. Collectively, the

331   non-reductive formation of these dissolved Fe species will favour the mobilisation and net loss of

332   heavier Fe isotopes from the sediment protolith. Previous studies have shown that NRD may only result

333   in small benthic Fe fluxes in some settings (Homoky et al., 2013), but fluxes out of the sediment may

334   be enhanced in locations of high volcanogenic (Homoky et al., 2011) and lithogenic (e.g. dust, riverine

335   particles) deposition and/or sediment re-suspension (Homoky et al., 2021; Klar et al., 2018; Labatut et

336   al., 2014; Lam et al., 2020).

337   The regular and large-scale input of tephra from volcanoes in Central America (e.g. Schindlbeck et al.,

338   2016), and the Lesser Antilles (Coussens et al., 2017; Palmer et al., 2016) provides a significant source

339   of volcanic material for the Caribbean Sea. In a similar manner to western Africa, where input of

340   lithogenic material via riverine input leads to a large supply of Fe from NRD (Klar et al., 2018), our

341   data suggest the deposition of tephra in the Caribbean may act as a source of Fe to seawater, via NRD.

342   Indeed, tephra is known to rapidly release Fe via interactions with seawater (Jones and Gislason, 2008),

343 and during early diagenesis (Longman et al., 2022, 2019). This release from tephra is inferred from the

344 relatively high Fe content in pore waters from U1396C (typical values between $10 - 50$ µmol; Fig. 2),

345 and dissolution of tephra is also reflected in the volcanogenic Sr isotope composition of the pore waters

346 (Fig. 4; Murray et al., 2018).

347 Further evidence for the non-reductive release of dFe from tephra in the marine sediments comes from

348 young tephra deposited in the Caribbean Sea and Holocene-aged volcanogenic turbidites deposited

349 around the Crozet Islands, Southern Ocean. An 18-month old tephra deposit sampled in deep-water off

350 Montserrat revealed the efficient consumption of pore water oxygen and high levels of dFe and dMn

351 (micro-molar concentrations) accumulated in pore waters in the absence of organic carbon to drive

352 bacterial metal reduction (Homoky et al., 2011). Hembury et al. (2012) attributed this oxygen

353 consumption in the tephra to reaction with inorganic minerals, consistent with the idea that high pore

354 water dFe and dMn contents resulted from the NRD of tephra in seawater rather than bacterial

355 dissimilatory reduction. Analogous, but Holocene-aged, volcanogenic turbidites around the Crozet

356 Islands also display micro-molar levels of dFe and dMn in pore waters, here present as colloids in the

357 presence of oxygen. A non-reductive provenance of dFe in pore water (and likely ligand binding) was

358 also confirmed by its $\delta^{56}Fe$ values between -0.01 and 0.12‰ (Homoky et al., 2011, 2009). Evidently,

359 we can expect to see comparative differences in the physical chemistry of dFe within marine sediments

360 due to variations in sediment and seawater admixtures and reaction times, but the primary, rapid and

361 non-reductive release of Fe from volcanic tephra during transport through the water column and after

362 deposition at the seafloor appears to be a defining characteristic of volcanic sedimentation elsewhere,

363 consistent with our findings. Evidence for the impact of NRD on regional Fe budgets might be identified

364 in $\delta^{56}Fe$ compositions of western North Atlantic seawater. For example, dissolved $\delta^{56}Fe$ values from

365 0.2 to 0.74‰ in seawater down to 4200 metres offshore Bermuda (Conway and John, 2014; John and

366 Adkins, 2012), are within the range we have calculated as $\delta^{56}Fe_{Lost}$ (Fig. 5). Presently, these Fe isotope

367 compositions are attributed to a mixture of dust fractionation and organic ligand-mediated processes

368 (Conway and John, 2014; John and Adkins, 2012; König et al., 2021). We suggest that input of dFe

369 from tephra-rich sediment alteration may also contribute to these isotopically heavy $\delta^{56}Fe$ values in the

370   Bermudan samples via the advection of benthic nepheloid layers that are thought to enter this region

371   from the Caribbean and Gulf of Mexico (Feely, 1975; McCave, 1986), but additional new analyses of

372   Caribbean Sea seawater may be needed to test this hypothesis.

373   ## 4. Conclusions

374   We measured the major and trace element concentration and Fe isotopic composition of tephra and

375   sediment layers from the Caribbean Sea. The bulk sediment is dominated by biogenic carbonate, but

376   using a multivariate partitioning approach, we determined that aluminosilicate material in the sediment

377   is a mixture of three primary sources, two linked to tephra deposition and one linked to terrestrial input.

378   Overall, dispersed tephra comprises 29% of all sediment analyzed in this study. Fe isotope analyses

379   indicate that tephra within the sediment, which has undergone water column transport and subsequent

380   diagenesis, has $\delta^{56}Fe$ values that are isotopically lighter than its source material, with $\delta^{56}Fe$ values as

381   low as -0.26‰. This value is considerably lighter than measured $\delta^{56}Fe$ from fresh tephra (which we

382   show to be close to 0 ‰). Modelling of these Fe isotope data using multivariate partitioning suggests

383   that the negative $\delta^{56}Fe$ values of sediment hosted tephra layers results from the preferential loss of heavy

384   Fe isotopes during diagenesis of tephra. This Fe loss most likely occurs as the result of non-reductive

385   dissolution of the silicate material and the mobilisation of tephra hosted Fe in a dissolved phase. We

386   suggest this tephra dissolution may provide an important source of dissolved Fe and possibly other

387   micro-nutrient elements for phytoplankton metabolism and marine biogeochemical cycles in the

388   vicinity of volcanoes. Further, the deposition and dissolution of volcanic material might be traced by

389   its influence on the mean isotope composition of dissolved Fe in seawater connected to regions of

390   volcanic sedimentation.

References

401   Abadie, C., Lacan, F., Radic, A., Pradoux, C., Poitrasson, F., 2017. Iron isotopes reveal distinct
402   dissolved iron sources and pathways in the intermediate versus deep Southern Ocean. Proc. Natl.
403   Acad. Sci. U. S. A. 114, 858–863. https://doi.org/10.1073/pnas.1603107114

404   Achterberg, E.P., Moore, C.M., Henson, S.A., Steigenberger, S., Stohl, A., Eckhardt, S., Avendano,
405   L.C., Cassidy, M., Hembury, D., Klar, J.K., Lucas, M.I., Macey, A.I., Marsay, C.M., Ryan-Keogh,
406   T.J., 2013. Natural iron fertilization by the Eyjafjallajökull volcanic eruption. Geophys. Res. Lett.
407   40, 921–926. https://doi.org/10.1002/grl.50221

408   Beard, B.L., Johnson, C.M., Von Damm, K.L., Poulson, R.L., 2003. Iron isotope constraints on Fe
409   cycling and mass balance in oxygenated Earth oceans. Geology 31, 629–632.
410   https://doi.org/10.1130/0091-7613(2003)031<0629:IICOFC>2.0.CO;2

411   Bennett, S.A., Rouxel, O., Schmidt, K., Garbe-Schönberg, D., Statham, P.J., German, C.R., 2009. Iron
412   isotope fractionation in a buoyant hydrothermal plume, 5°S Mid-Atlantic Ridge. Geochim.
413   Cosmochim. Acta 73, 5619–5634. https://doi.org/10.1016/J.GCA.2009.06.027

414   Böning, P., Brumsack, H.J., Böttcher, M.E., Schnetger, B., Kriete, C., Kallmeyer, J., Borchers, S.L.,
415   2004. Geochemistry of Peruvian near-surface sediments. Geochim. Cosmochim. Acta 68, 4429–
416   4451. https://doi.org/10.1016/j.gca.2004.04.027

417   Böning, P., Schnetger, B., Belz, L., Ferdelman, T., Brumsack, H.J., Pahnke, K., 2020. Sedimentary iron
418   cycling in the Benguela upwelling system off Namibia. Earth Planet. Sci. Lett. 538, 116212.
419   https://doi.org/10.1016/J.EPSL.2020.116212

420   Boyle, E.A., 1981. Cadmium, zinc, copper, and barium in foraminifera tests. Earth Planet. Sci. Lett. 53,
421   11–35. https://doi.org/10.1016/0012-821X(81)90022-4

422   Browning, T.J., Achterberg, E.P., Engel, A., Mawji, E., 2021. Manganese co-limitation of
423   phytoplankton growth and major nutrient drawdown in the Southern Ocean. Nat. Commun. 12,
424   1–9. https://doi.org/10.1038/s41467-021-21122-6

425   Browning, T.J., Bouman, H.A., Henderson, G.M., Mather, T.A., Pyle, D.M., Schlosser, C., Woodward,
426   E.M.S., Moore, C.M., 2014. Strong responses of Southern Ocean phytoplankton communities to
427   volcanic ash. Geophys. Res. Lett. 41, 2851–2857. https://doi.org/10.1002/2014GL059364

428   Conway, T.M., John, S.G., 2014. Quantification of dissolved iron sources to the North Atlantic Ocean.
429   Nature 511, 212–215. https://doi.org/10.1038/nature13482

430   Coussens, M., Cassidy, M., Watt, S.F.L., Jutzeler, M., Talling, P.J., Barfod, D., Gernon, T.M., Taylor,
431   R., Hatter, S.J., Palmer, M.R., 2017. Long-term changes in explosive and effusive behaviour at
432   andesitic arc volcanoes: Chronostratigraphy of the Centre Hills Volcano, Montserrat. J. Volcanol.
433   Geotherm. Res. 333–334, 15–35. https://doi.org/10.1016/j.jvolgeores.2017.01.003

434   Dauphas, N., Pourmand, A., Teng, F.Z., 2009. Routine isotopic analysis of iron by HR-MC-ICPMS:
435   How precise and how accurate? Chem. Geol. 267, 175–184.
436   https://doi.org/10.1016/J.CHEMGEO.2008.12.011

437 Dideriksen, K., Baker, J.A., Stipp, S.L.S., 2008. Equilibrium Fe isotope fractionation between inorganic
438 aqueous Fe(III) and the siderophore complex, Fe(III)-desferrioxamine B. Earth Planet. Sci. Lett.
439 269, 280–290. https://doi.org/10.1016/J.EPSL.2008.02.022

440 Duggen, S., Olgun, N., Croot, P., Hoffmann, L., Dietze, H., Delmelle, P., Teschner, C., 2010. The role
441 of airborne volcanic ash for the surface ocean biogeochemical iron-cycle: a review.
442 Biogeosciences 7, 827–844. https://doi.org/10.5194/bg-7-827-2010

443 Dunlea, A.G., Murray, R.W., 2015. Optimization of end-members used in multiple linear regression
444 geochemical mixing models. Geochemistry, Geophys. Geosystems 16, 4021–4027.
445 https://doi.org/10.1002/2015GC006132

446 Dunlea, A.G., Murray, R.W., Sauvage, J., Spivack, A.J., Harris, R.N., D'Hondt, S., 2015. Dust, volcanic
447 ash, and the evolution of the South Pacific Gyre through the Cenozoic. Paleoceanography 30,
448 1078–1099. https://doi.org/10.1002/2015PA002829

449 Falkowski, P.G., Barber, R.T., Smetacek, V., 1998. Biogeochemical controls and feedbacks on ocean
450 primary production. Science (80-.). https://doi.org/10.1126/science.281.5374.200

451 Feely, R.A., 1975. Major-element composition of the particulate matter in the near-bottom nepheloid
452 layer of the gulf of Mexico. Mar. Chem. 3, 121–156. https://doi.org/10.1016/0304-
453 4203(75)90019-5

454 Foden, J., Sossi, P.A., Nebel, O., 2018. Controls on the iron isotopic composition of global arc magmas.
455 Earth Planet. Sci. Lett. 494, 190–201. https://doi.org/10.1016/J.EPSL.2018.04.039

456 Frogner, P., Reynir Gíslason, S., Óskarsson, N., 2001. Fertilizing potential of volcanic ash in ocean
457 surface water. Geology 29, 487. https://doi.org/10.1130/0091-
458 7613(2001)029<0487:FPOVAI>2.0.CO;2

459 Goñi, M.A., Teixeira, M.J., Perkeya, D.W., 2003. Sources and distribution of organic matter in a river-
460 dominated estuary (Winyah Bay, SC, USA). Estuar. Coast. Shelf Sci. 57, 1023–1048.
461 https://doi.org/10.1016/S0272-7714(03)00008-8

462 González De Vega, C., Chernonozhkin, S.M., Grigoryan, R., Costas-Rodríguez, M., Vanhaecke, F.,
463 2020. Characterization of the new isotopic reference materials IRMM-524A and ERM-AE143 for
464 Fe and Mg isotopic analysis of geological and biological samples. J. Anal. At. Spectrom. 35,
465 2517–2529. https://doi.org/10.1039/D0JA00225A

466 Hembury, D.J., Palmer, M.R., Fones, G.R., Mills, R.A., Marsh, R., Jones, M.T., 2012. Uptake of
467 dissolved oxygen during marine diagenesis of fresh volcanic material. Geochim. Cosmochim.
468 Acta 84, 353–368. https://doi.org/10.1016/J.GCA.2012.01.017

469 Homoky, W.B., Conway, T.M., John, S.G., König, D., Deng, F.F., Tagliabue, A., Mills, R.A., 2021.
470 Iron colloids dominate sedimentary supply to the ocean interior. Proc. Natl. Acad. Sci. U. S. A.
471 118. https://doi.org/10.1073/PNAS.2016078118

472 Homoky, W.B., Hembury, D.J., Hepburn, L.E., Mills, R.A., Statham, P.J., Fones, G.R., Palmer, M.R.,
473 2011. Iron and manganese diagenesis in deep sea volcanogenic sediments and the origins of pore
474 water colloids. Geochim. Cosmochim. Acta 75, 5032–5048.
475 https://doi.org/10.1016/J.GCA.2011.06.019

476 Homoky, W.B., John, S.G., Conway, T.M., Mills, R.A., 2013. Distinct iron isotopic signatures and
477 supply from marine sediment dissolution. Nat. Commun. 4, 1–10.
478 https://doi.org/10.1038/ncomms3143

479 Homoky, W.B., Severmann, S., Mills, R.A., Statham, P.J., Fones, G.R., 2009. Pore-fluid Fe isotopes
480 reflect the extent of benthic Fe redox recycling: Evidence from continental shelf and deep-sea
481 sediments. Geology 37, 751–754. https://doi.org/10.1130/G25731A.1

482 Ilina, S.M., Poitrasson, F., Lapitskiy, S.A., Alekhin, Y. V., Viers, J., Pokrovsky, O.S., 2013. Extreme
483   iron isotope fractionation between colloids and particles of boreal and temperate organic-rich
484   waters. Geochim. Cosmochim. Acta 101, 96–111. https://doi.org/10.1016/J.GCA.2012.10.023

485 John, S.G., Adkins, J., 2012. The vertical distribution of iron stable isotopes in the North Atlantic near
486   Bermuda. Global Biogeochem. Cycles 26, 2034. https://doi.org/10.1029/2011GB004043

487 Johnson, C., Beard, B., Weyer, S., 2020. Iron Geochemistry: An Isotopic Perspective.

488 Jones, M.T., Gislason, S.R., 2008. Rapid releases of metal salts and nutrients following the deposition
489   of volcanic ash into aqueous environments. Geochim. Cosmochim. Acta 72, 3661–3680.
490   https://doi.org/10.1016/j.gca.2008.05.030

491 Klar, J.K., Schlosser, C., Milton, J.A., Woodward, E.M.S., Lacan, F., Parkinson, I.J., Achterberg, E.P.,
492   James, R.H., 2018. Sources of dissolved iron to oxygen minimum zone waters on the Senegalese
493   continental margin in the tropical North Atlantic Ocean: Insights from iron isotopes. Geochim.
494   Cosmochim. Acta 236, 60–78. https://doi.org/10.1016/j.gca.2018.02.031

495 Kolber, Z.S., Barber, R.T., Coale, K.H., Fitzwateri, S.E., Greene, R.M., Johnson, K.S., Lindley, S.,
496   Falkowski, P.G., 1994. Iron limitation of phytoplankton photosynthesis in the equatorial Pacific
497   Ocean. Nature 371, 145–149. https://doi.org/10.1038/371145a0

498 König, D., Conway, T.M., Ellwood, M.J., Homoky, W.B., Tagliabue, A., 2021. Constraints on the
499   Cycling of Iron Isotopes From a Global Ocean Model. Global Biogeochem. Cycles 35,
500   e2021GB006968. https://doi.org/10.1029/2021GB006968

501 Labatut, M., Lacan, F., Pradoux, C., Chmeleff, J., Radic, A., Murray, J.W., Poitrasson, F., Johansen,
502   A.M., Thil, F., 2014. Iron sources and dissolved-particulate interactions in the seawater of the
503   Western Equatorial Pacific, iron isotope perspectives. Global Biogeochem. Cycles 28, 1044–1065.
504   https://doi.org/10.1002/2014GB004928

505 Lam, P.J., Heller, M.I., Lerner, P.E., Moffett, J.W., Buck, K.N., 2020. Unexpected Source and
506   Transport of Iron from the Deep Peru Margin. ACS Earth Sp. Chem. 4, 977–992.
507   https://doi.org/10.1021/ACSEARTHSPACECHEM.0C00066/ASSET/IMAGES/LARGE/SP0C0
508   0066_0009.JPEG

509 Le Friant, A., Ishizuka, O., Stroncik, N.A., Expedition 340 Scientists, T., 2013. Proc. IODP, 340.
510   Integrated Ocean Drilling Program Management International, Inc., Tokyo.

511 Lee, C.-T.A., Jiang, H., Ronay, E., Minisini, D., Stiles, J., Neal, M., 2018. Volcanic ash as a driver of
512   enhanced organic carbon burial in the Cretaceous. Sci. Rep. 8, 4197.
513   https://doi.org/10.1038/s41598-018-22576-3

514 Liu, S.A., Teng, F.Z., Li, S., Wei, G.J., Ma, J.L., Li, D., 2014. Copper and iron isotope fractionation
515   during weathering and pedogenesis: Insights from saprolite profiles. Geochim. Cosmochim. Acta
516   146, 59–75. https://doi.org/10.1016/J.GCA.2014.09.040

517 Longman, J., Mills, B.J.W., Manners, H.R., Gernon, T.M., Palmer, M.R., 2021. Late Ordovician climate
518   change and extinctions driven by elevated volcanic nutrient supply. Nat. Geosci. 14, 924–929.
519   https://doi.org/10.1038/s41561-021-00855-5

520 Longman, J., Palmer, M.R., Gernon, T.M., 2020. Viability of greenhouse gas removal via artificial
521   addition of volcanic ash to the ocean. Anthropocene 32.
522   https://doi.org/10.1016/j.ancene.2020.100264

523 Longman, J., Palmer, M.R., Gernon, T.M., Manners, H.R., 2019. The role of tephra in enhancing
524   organic carbon preservation in marine sediments. Earth-Science Rev. 192, 480–490.
525   https://doi.org/10.1016/j.earscirev.2019.03.018

526 Longman, J., Palmer, M.R., Gernon, T.M., Manners, H.R., Jones, M.T., 2022. Subaerial volcanism as

527   a major contributor to oceanic iron and manganese cycles. Commun. Earth Environ.

528   Lough, A.J.M., Klar, J.K., Homoky, W.B., Comer-Warner, S.A., Milton, J.A., Connelly, D.P., James,
529   R.H., Mills, R.A., 2017. Opposing authigenic controls on the isotopic signature of dissolved iron
530   in   hydrothermal   plumes.   Geochim.   Cosmochim.   Acta   202,   1–20.
531   https://doi.org/10.1016/J.GCA.2016.12.022

532   Martin, J.H., Fitzwater, S.E., 1988. Iron deficiency limits phytoplankton growth in the north-east pacific
533   subarctic. Nature 331, 341–343. https://doi.org/10.1038/331341a0

534   Maters, E.C., Delmelle, P., Gunnlaugsson, H.P., 2017. Controls on iron mobilisation from volcanic ash
535   at low pH: Insights from dissolution experiments and Mössbauer spectroscopy. Chem. Geol. 449,
536   73–81. https://doi.org/10.1016/J.CHEMGEO.2016.11.036

537   McCave, I.N., 1986. Local and global aspects of the bottom nepheloid layers in the world ocean.
538   Netherlands J. Sea Res. 20, 167–181. https://doi.org/10.1016/0077-7579(86)90040-2

539   Moore, C.M., Mills, M.M., Arrigo, K.R., Berman-Frank, I., Bopp, L., Boyd, P.W., Galbraith, E.D.,
540   Geider, R.J., Guieu, C., Jaccard, S.L., Jickells, T.D., La Roche, J., Lenton, T.M., Mahowald, N.M.,
541   Marañón, E., Marinov, I., Moore, J.K., Nakatsuka, T., Oschlies, A., Saito, M.A., Thingstad, T.F.,
542   Tsuda, A., Ulloa, O., 2013. Processes and patterns of oceanic nutrient limitation. Nat. Geosci. 6,
543   701–710. https://doi.org/10.1038/ngeo1765

544   Morgan, J.L.L., Wasylenki, L.E., Nuester, J., Anbar, A.D., 2010. Fe Isotope Fractionation during
545   Equilibration   of   Fe−Organic   Complexes.   Environ.   Sci.   Technol.   44,   6095–6101.
546   https://doi.org/10.1021/ES100906Z

547   Murray, N.A., McManus, J., Palmer, M.R., Haley, B., Manners, H., 2018. Diagenesis in tephra-rich
548   sediments from the Lesser Antilles Volcanic Arc: Pore fluid constraints. Geochim. Cosmochim.
549   Acta 228, 119–135. https://doi.org/10.1016/J.GCA.2018.02.039

550   Murray, N.A., Muratli, J.M., Hartwell, A.M., Manners, H., Megowan, M.R., Goñi, M., Palmer, M.,
551   McManus, J., 2016. Data report: dissolved minor element compositions, sediment major and
552   minor element concentrations, and reactive iron and manganese data from the Lesser Antilles
553   volcanic arc region, IODP Expedition 340 Sites U1394, U1395, U1396, U1399, and U1400. Proc.
554   Integr. Ocean Drill. Progr. 340. https://doi.org/10.2204/iodp.proc.340.207.2016

555   Oeser, M., Weyer, S., Horn, I., Schuth, S., 2014. High-Precision Fe and Mg Isotope Ratios of Silicate
556   Reference Glasses Determined In Situ by Femtosecond LA-MC-ICP-MS and by Solution
557   Nebulisation   MC-ICP-MS.   Geostand.   Geoanalytical   Res.   38,   311–328.
558   https://doi.org/10.1111/J.1751-908X.2014.00288.X

559   Olgun, N., Duggen, S., Croot, P.L., Delmelle, P., Dietze, H., Schacht, U., Óskarsson, N., Siebe, C.,
560   Auer, A., Garbe-Schönberg, D., 2011. Surface ocean iron fertilization: The role of airborne
561   volcanic ash from subduction zone and hot spot volcanoes and related iron fluxes into the Pacific
562   Ocean. Global Biogeochem. Cycles 25, n/a-n/a. https://doi.org/10.1029/2009GB003761

563   Olgun, N., Duggen, S., Langmann, B., Hort, M., Waythomas, C., Hoffmann, L., Croot, P., 2013.
564   Geochemical evidence of oceanic iron fertilization by the Kasatochi volcanic eruption in 2008 and
565   the potential impacts on Pacific sockeye salmon. Mar. Ecol. Prog. Ser. 488, 81–88.
566   https://doi.org/10.3354/meps10403

567   Palmer, M.R., Hatter, S.J., Gernon, T.M., Taylor, R.N., Cassidy, M., Johnson, P., Le Friant, A.,
568   Ishizuka, O., 2016. Discovery of a large 2.4 Ma Plinian eruption of Basse-Terre, Guadeloupe,
569   from the marine sediment record. Geology 44, 123–126. https://doi.org/10.1130/G37193.1

570   Peters, J.L., Murray, R.W., Sparks, J.W., Coleman, D.S., Leckie, R.M., Sigurdsson, H., Acton, G.D.,
571   Abrams, L.J., Bralower, T.J., Carey, S.N., Chaisson, W.P., Cotillon, P., Cunningham, A.D.,
572   D'Hondt, S.L., Droxler, A.W., Galbrun, B., Gonzalez, J., Haug, G.H., Kameo, K., King, J.W.,

Lind, I.L., Louvel, V., Lyons, T.W., Mutti, M., Myers, G., Pearce, R.B., Pearson, D.G., Peterson, L.C., Roehl, U., 2000. Terrigenous matter and dispersed ash in sediment from the Caribbean Sea; results from Leg 165. Proc. Ocean Drill. Program, Sci. Results 165, 115–124. https://doi.org/10.2973/odp.proc.sr.165.003.2000

Pisias, N.G., Murray, R.W., Scudder, R.P., 2013. Multivariate statistical analysis and partitioning of sedimentary geochemical data sets: General principles and specific MATLAB scripts. Geochemistry, Geophys. Geosystems 14, 4015–4020. https://doi.org/10.1002/ggge.20247

Pyle, D.M., 1995. Mass and energy budgets of explosive volcanic eruptions. Geophys. Res. Lett. 22, 563–566. https://doi.org/10.1029/95GL00052

Radic, A., Lacan, F., Murray, J.W., 2011. Iron isotopes in the seawater of the equatorial Pacific Ocean: New constraints for the oceanic iron cycle. Earth Planet. Sci. Lett. 306, 1–10. https://doi.org/10.1016/j.epsl.2011.03.015

Reid, R.P., Carey, S.N., Ross, D.R., 1996. Late Quaternary sedimentation in the Lesser Antilles island arc. Bull. Geol. Soc. Am. 108, 78–100. https://doi.org/10.1130/0016-7606(1996)108<0078:LQSITL>2.3.CO;2

Rudnick, R.L., Gao, S., 2013. Composition of the Continental Crust. Treatise Geochemistry Second Ed. 4, 1–51. https://doi.org/10.1016/B978-0-08-095975-7.00301-6

Schindlbeck, J.C., Kutterolf, S., Freundt, A., Alvarado, G.E., Wang, K. -L., Straub, S.M., Hemming, S.R., Frische, M., Woodhead, J.D., 2016. Late Cenozoic tephrostratigraphy offshore the southern Central American Volcanic Arc: 1. Tephra ages and provenance. Geochemistry, Geophys. Geosystems 17, 4641–4668. https://doi.org/10.1002/2016GC006503@10.1002/(ISSN)1525-2027.SUBDUCT2

Schindlbeck, J.C., Kutterolf, S., Freundt, A., Eisele, S., Wang, K.-L., Frische, M., 2018. Miocene to Holocene Marine Tephrostratigraphy Offshore Northern Central America and Southern Mexico: Pulsed Activity of Known Volcanic Complexes. Geochemistry, Geophys. Geosystems 19, 4143–4173. https://doi.org/10.1029/2018GC007832

Schoenberg, R., Von Blanckenburg, F., 2005. An assessment of the accuracy of stable Fe isotope ratio measurements on samples with organic and inorganic matrices by high-resolution multicollector ICP-MS. Int. J. Mass Spectrom. 242, 257–272. https://doi.org/10.1016/J.IJMS.2004.11.025

Scudder, R.P., Murray, R.W., Plank, T., 2009. Dispersed ash in deeply buried sediment from the northwest Pacific Ocean: An example from the Izu–Bonin arc (ODP Site 1149). Earth Planet. Sci. Lett. 284, 639–648. https://doi.org/10.1016/J.EPSL.2009.05.037

Scudder, R.P., Murray, R.W., Schindlbeck, J.C., Kutterolf, S., Hauff, F., McKinley, C.C., 2014. Regional-scale input of dispersed and discrete volcanic ash to the Izu-Bonin and Mariana subduction zones. Geochemistry, Geophys. Geosystems 15, 4369–4379. https://doi.org/10.1002/2014GC005561

Scudder, R.P., Murray, R.W., Schindlbeck, J.C., Kutterolf, S., Hauff, F., Underwood, M.B., Gwizd, S., Lauzon, R., McKinley, C.C., 2016. Geochemical approaches to the quantification of dispersed volcanic ash in marine sediment. Prog. Earth Planet. Sci. 3, 1. https://doi.org/10.1186/s40645-015-0077-y

Simonella, L.E., Palomeque, M.E., Croot, P.L., Stein, A., Kupczewski, M., Rosales, A., Montes, M.L., Colombo, F., García, M.G., Villarosa, G., Gaiero, D.M., 2015. Soluble iron inputs to the Southern Ocean through recent andesitic to rhyolitic volcanic ash eruptions from the Patagonian Andes. Global Biogeochem. Cycles 29, 1125–1144. https://doi.org/10.1002/2015GB005177

Tagliabue, A., Aumont, O., Death, R., Dunne, J.P., Dutkiewicz, S., Galbraith, E., Misumi, K., Moore, J.K., Ridgwell, A., Sherman, E., Stock, C., Vichi, M., Völker, C., Yool, A., 2016. How well do

619   global ocean biogeochemistry models simulate dissolved iron distributions? Global Biogeochem.
620   Cycles 30, 149–174. https://doi.org/10.1002/2015GB005289

621 Tagliabue, A., Bowie, A.R., Boyd, P.W., Buck, K.N., Johnson, K.S., Saito, M.A., 2017. The integral
622   role of iron in ocean biogeochemistry. Nature. https://doi.org/10.1038/nature21058

623 Weyer, S., Schwieters, J.B., 2003. High precision Fe isotope measurements with high mass resolution
624   MC-ICPMS. Int. J. Mass Spectrom. 226, 355–368. https://doi.org/10.1016/S1387-
625   3806(03)00078-2
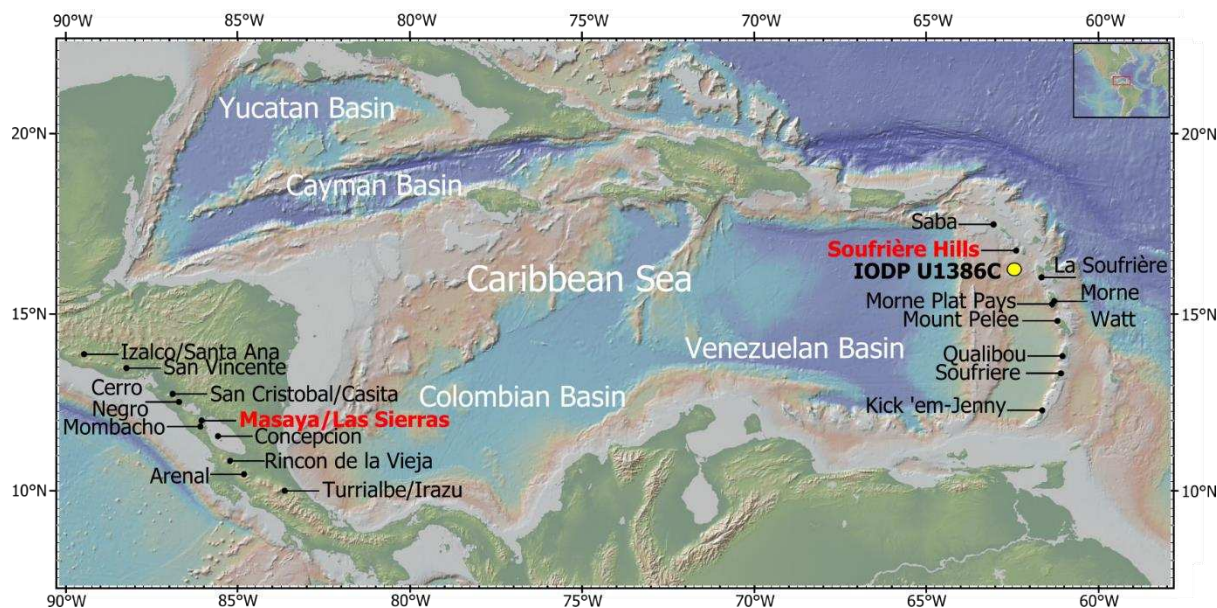
Figures


Figure 1: Map indicating location of Hole U1396C (yellow circle) within the Caribbean Sea area. Also shown are the locations of the primary recently active volcanoes in the region. The location of Las Sierras, and Soufrière Hills volcanoes, used in the modelling here, are indicated by bold red text. Map created in ArcMap 10.3, Environmental Systems Resource Institute, ArcMap 10.3 ESRI, Redlands, California, http://desktop.arcgis.com/en/arcmap/.
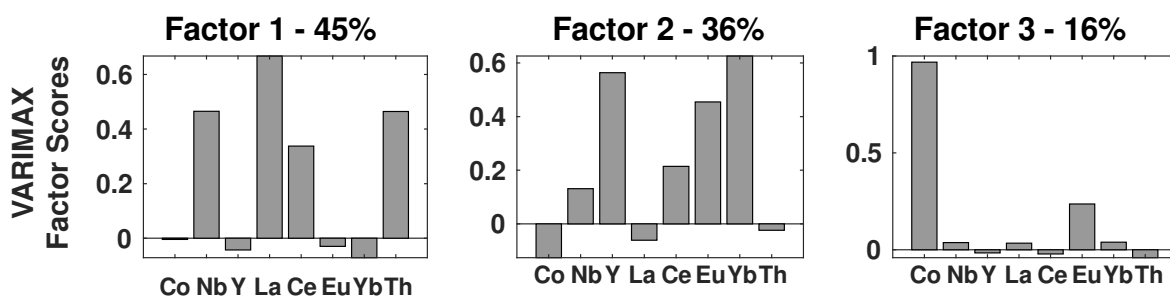
Figure 2: The VARIMAX factor scores from the Q-mode factor analysis. Elements affiliated with the

635   aluminosilicate fraction produced three factors that explain 97% of the variability of the dataset (45%,

636   36%, and 16%, respectively).

637
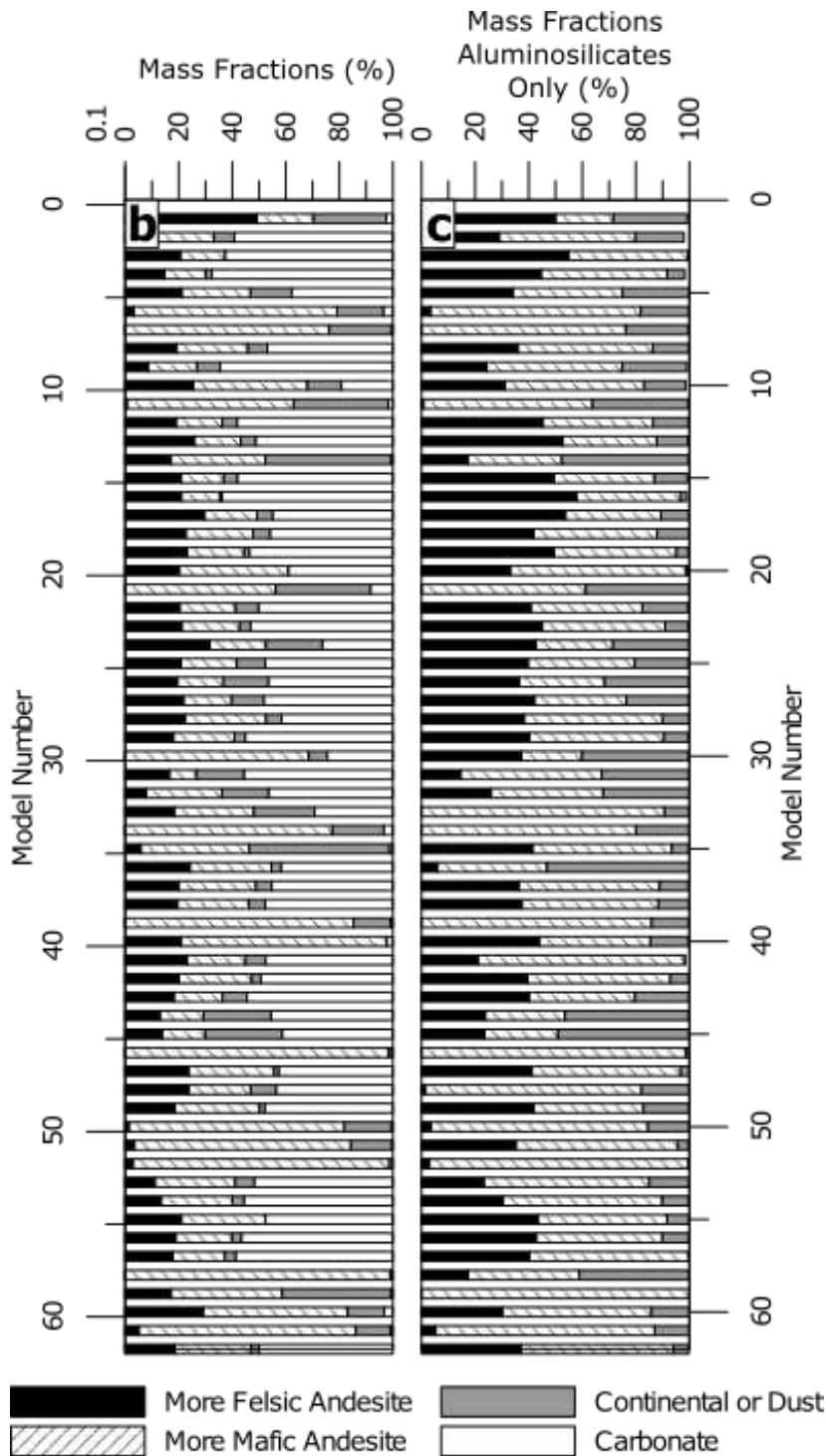
Figure 3: a) The results of the CLS model. Modelled end-member mass fractions in each discrete layer

639   or bulk sediment sample plotted with the same scale as panel a. Black and hashed white indicate the

mass fractions of the more felsic and more mafic andesites, respectively. Grey represents contributions from an upper continental crust or dust source. The remaining white area represents the carbonate fraction of bulk sediment. b) The CLS modelled mass fractions of only the aluminosilicate fraction of the samples (excluding the carbonate fraction).
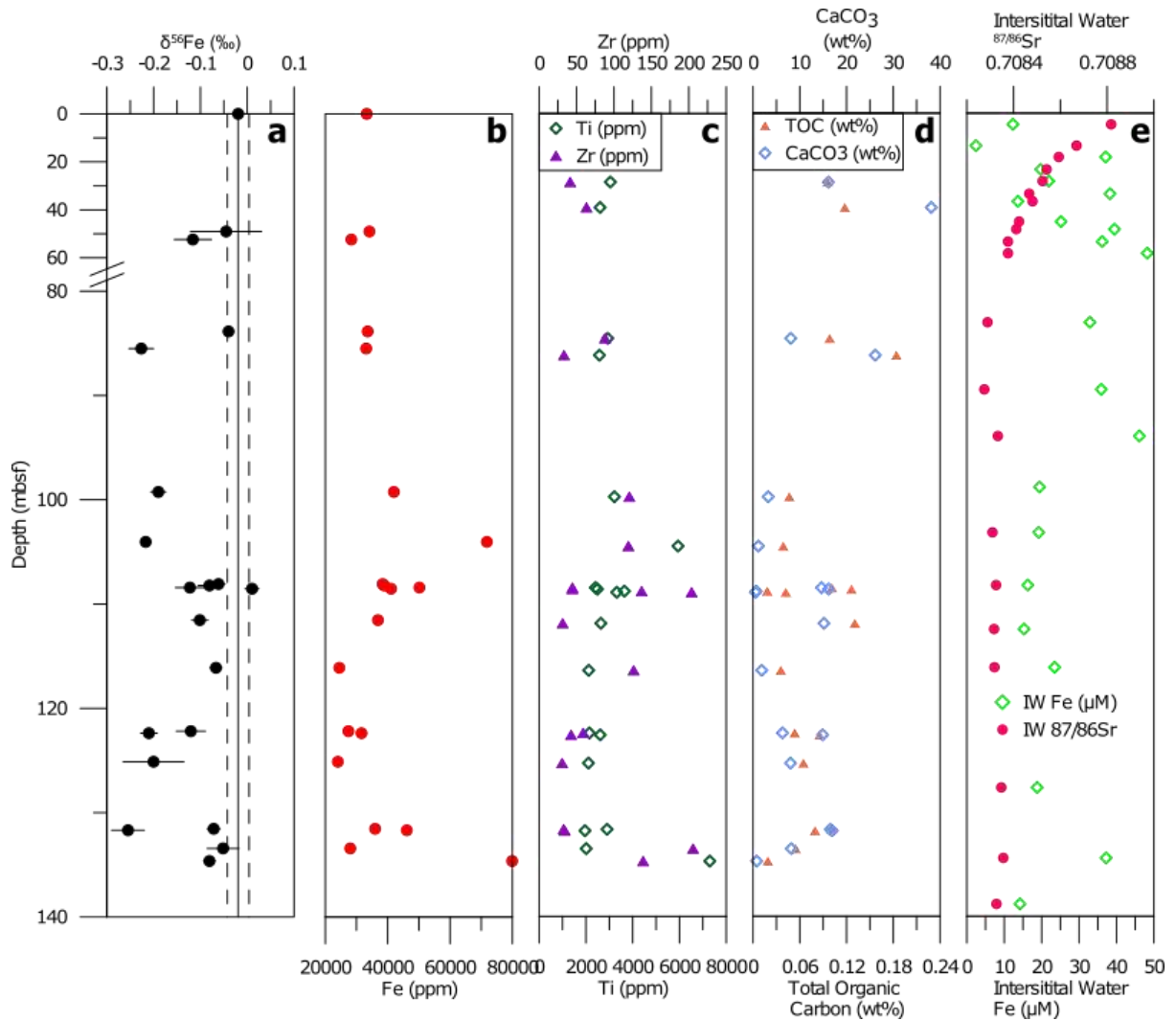

Figure 4: Geochemical parameters from U1396C. (a) Fe isotope composition of analysed samples, with error bars indicating measurement error (2SD). The measured value of terrestrially emplaced ash from Montserrat indicated with a black line, with measurement error indicated by dashed lines. (b) Fe content of samples analysed for isotopic composition. (c) Ti and Zr content for the same samples. (d) calcium carbonate and organic carbon (total carbon) content for the same samples. (e) Interstitial water Fe content and Sr isotope composition (from Murray et al., 2018).
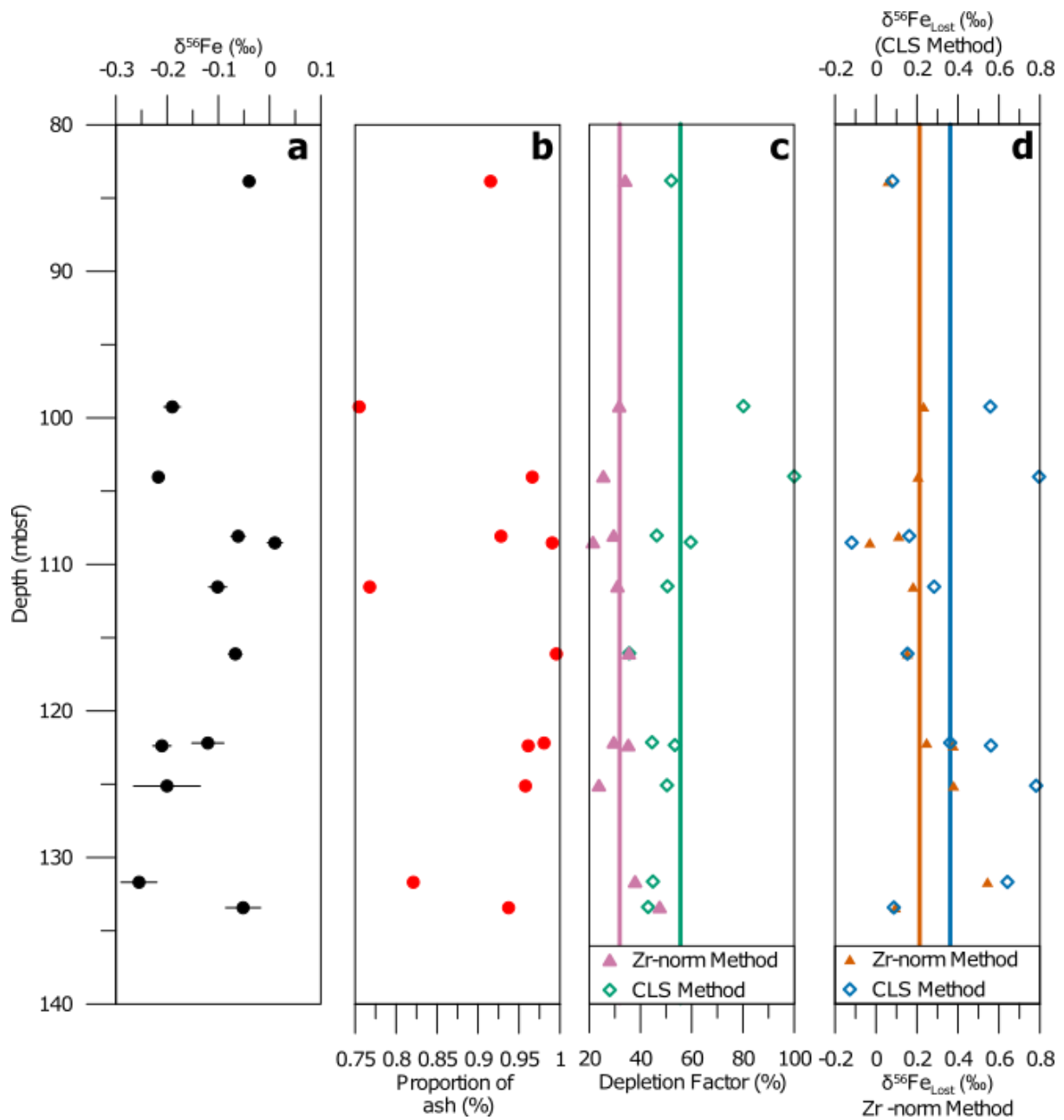
Figure 5: Parameters used in the mass balance modelling of the lost Fe fraction ($\delta^{56}Fe_{Lost}$), or the isotopic composition of Fe flux from samples with >75% tephra. (a) Bulk $\delta^{56}Fe$ measurements for the samples with high enough ash content to be modelled (>75%). (b) The proportion of ash in each sample, as calculated from the multivariate modelling. (c) Fe depletion factor (DF) calculations, DF Method 1 from Lee et al. (2018) and DF Method 2 from our multivariate partitioning. Individual models are

660   indicated with coloured symbols, and the mean of each method is highlighted with a coloured line. (d)

661   The calculated $\delta^{56}Fe_{Lost}$ for each of the samples, with the calculations made using the depletion factors

662   displayed in panel c. Again, the mean of the outputs is highlighted with a coloured line.